European Journal of Mechanics B/Fluids 40 (2013) 64–74

Contents lists available at SciVerse ScienceDirect

European Journal of Mechanics B/Fluids

journal homepage: www.elsevier.com/locate/ejmflu

Shock-induced collapse of a bubble inside a deformable vessel

Vedran Coralic *, Tim Colonius [1]

Division of Engineering and Applied Science, California Institute of Technology, Pasadena, CA 91125, USA

ARTICLE INFO

Article history:
Available online 17 January 2013

Keywords:
Shockwave lithotripsy
Cavitation bubbles
Gas bubbles
Shock-induced collapse
Vessel rupture
Renal injury

ABSTRACT

Shockwave lithotripsy repeatedly focuses shockwaves on kidney stones to induce their fracture, partially through cavitation erosion. A typical side effect of the procedure is hemorrhage, which is potentially the result of the growth and collapse of bubbles inside blood vessels. To identify the mechanisms by which shock-induced collapse could lead to the onset of injury, we study an idealized problem involving a preexisting bubble in a deformable vessel. We utilize a high-order accurate, shock- and interface-capturing, finite-volume scheme and simulate the three-dimensional shock-induced collapse of an air bubble immersed in a cylindrical water column which is embedded in a gelatin/water mixture. The mixture is a soft tissue simulant, 10% gelatin by weight, and is modeled by the stiffened gas equation of state. The bubble dynamics of this model configuration are characterized by the collapse of the bubble and its subsequent jetting in the direction of the propagation of the shockwave. The vessel wall, which is defined by the material interface between the water and gelatin/water mixture, is invaginated by the collapse and distended by the impact of the jet. The present results show that the highest measured pressures and deformations occur when the volumetric confinement of the bubble is strongest, the bubble is nearest the vessel wall and/or the angle of incidence of the shockwave reduces the distance between the jet tip and the nearest vessel surface. For a particular case considered, the 40 MPa shockwave utilized in this study to collapse the bubble generated a vessel wall pressure of almost 450 MPa and produced both an invagination and distention of nearly 50% of the initial vessel radius on a $\mathcal{O}(10)$ ns timescale. These results are indicative of the significant potential of shock-induced collapse to contribute to the injury of blood vessels in shockwave lithotripsy.

1. Introduction

Shockwave lithotripsy (SWL) is a medical procedure to eliminate kidney stones. In typical clinical applications, approximately 2000 pressure pulses, with peak positive pressures between 30 and 110 MPa and peak negative pressures between −5 and −15 MPa, are generated by the lithotripter [1]. These pulses, or shockwaves, are focused at the location of the stones in order to pulverize them and enable their expulsion through the urinary tract. Both the effectiveness and safety of the treatment depend on, among other factors, the bubble dynamics excited by the passage of the shockwaves. Cavitating bubbles are documented to occur during treatment in both urine and surrounding tissue [2]. In the vicinity of kidney stones, cavitation erosion is thought to be an important mechanism of stone comminution and is characterized by the formation of liquid jets and the emission of shockwaves, both with the potential to inflict significant damage to nearby stones [3–5]. Unfortunately, cavitation in SWL is also implicated in the onset of renal trauma, specifically hemorrhage, which is instigated by the rupture of small blood vessels, such as capillaries, arterioles and venules, which range from 5 to 100 μm in diameter [1,6,7]. Recent experiments in the vasculature of *ex vivo* rat mesentery suggest that the growth and collapse of bubbles, along with liquid jet impact, may deform small blood vessels sufficiently as to cause them to rupture [8–10]. In order to improve the effectiveness and safety of SWL, it is therefore imperative to fully understand the mechanisms through which cavitation may contribute to both stone removal and vascular injury.

In both experiments and simulations, characterization of bubble–vessel dynamics has been difficult. Experimentally, the challenges of performing measurements and observations in tissue and blood vessels are exacerbated by small spatial and fast temporal scales. As a result, experimental work has primarily been carried out *in vitro*, typically utilizing gels and vessel phantoms to model tissue and blood vessels, respectively [7,11–13]. The first observations of *ex vivo* bubble dynamics in blood vessels and under clinical conditions were reported by Caskey et al. [14], in the case of ultrasonic cavitation of microbubbles in rat cecum. Their results were cast in the context of gene therapy and localized drug delivery and did not specifically address the potential mechanisms

* Corresponding author. Tel.: +1 626 395 4128.
E-mail addresses: vcoralic@caltech.edu (V. Coralic), colonius@caltech.edu (T. Colonius).
[1] Tel.: +1 626 395 4021; fax: +1 626 568 2719.

0997-7546/$ – see front matter
doi:10.1016/j.euromechflu.2013.01.003

of vascular injury. These mechanisms were the focus of subsequent work by Chen et al. [8–10], who performed analogous experiments in *ex vivo* rat mesentery. Utilizing high-speed microphotography, they measured the transient bubble–vessel interactions. They concluded that in the context of SWL, three mechanisms can potentially result in the mechanical failure of blood vessels due to cavitation. These include vessel distention due to bubble growth, vessel invagination due to bubble collapse, and finally, puncturing of the vessel wall due to bubble jetting.

Identifying these same mechanisms in numerical simulations has its own set of challenges. In particular, the understanding of the rheology of tissue is incomplete. Recent efforts to study vessel rupture mechanisms due to cavitating bubbles have circumvented this issue, modeling the wall of the blood vessel in great detail and omitting the tissue in which it is embedded. These simulations, performed by Ye and Bull [15] and Miao et al. [16], were carried out in an axisymmetric geometry, with both the bubble and vessel wall immersed in an incompressible fluid. Their efforts were successful in demonstrating that ultrasonically excited microbubbles could generate sufficiently high vessel wall stresses during distention as to induce rupture. Unfortunately, due to the axisymmetry and incompressibility assumptions, the wall stresses that would arise from bubble collapse and liquid jet impact could not be addressed.

The damage potential of bubble jetting was considered in the axisymmetric compressible flow simulations of Freund et al. [17] and Kobayashi et al. [18], but in the context of the shock-induced collapse of a bubble near a soft tissue simulant. Freund et al. set the properties of the simulant to those of water but varied its shear viscosity in order to study how effectively the various measurements of the viscous coefficient of tissue could suppress the penetration of the liquid jet. Coefficients between 0.01 and 10 Pa·s were considered. The results of the study showed that the penetration depth of the jet into the boundary could greatly be suppressed by the higher measurements of the tissue viscosity. The resulting viscous shear stresses, however, were estimated to be sufficiently large on the surface of the tissue as to potentially damage cells. Freund et al. postulated that this mechanism could be responsible for the observed damage to the endothelium, a thin layer of cells that lines the inner surface of a vessel wall. Kobayashi et al., on the other hand, presumed that such insult to tissue could occur due to the jetting of the bubble. They characterized the injury mechanism by correlating the deformation of the tissue boundary with the impulse that is generated by the water-hammer shockwave emitted during the formation of the liquid jet. Several soft tissues and soft tissue simulants were considered, including fat, liver and a gelatin/water mixture, and were modeled by the stiffened gas equation of state by fitting the density and acoustic impedance.

In this study, we build upon the computational efforts of Freund et al. and Kobayashi et al. and analyze the three-dimensional (3D) shock-induced collapse of an air bubble inside a cylindrical water column that is embedded in a 10% by weight gelatin/water mixture. This mixture, from here on, will simply be referred to as 10% gelatin. The problem setup is designed to emulate the shock-induced collapse of a preexisting gas bubble located inside a blood vessel surrounded by tissue. At this time, the viscoelastic properties of tissue are neglected and the vessel wall is treated as a material interface between the water and 10% gelatin. To our knowledge, the fully asymmetric and compressible bubble–vessel dynamics have never previously been reported in literature, so that this represents a first effort at their analysis.

Our study is broken up as follows. In Section 2, we discuss and justify the physical model utilized in the simulation of the bubble–vessel dynamics. In Section 3, we present the numerical scheme and its adaptation to the equations of motion of the physical model. The results of the simulations are analyzed and discussed in Section 4. Parametric variations in vessel confinement, bubble proximity and shockwave angle are presented and the pressures and deformations to which the vessel wall is subjected are quantified and cast in the context of the potential for vascular injury to occur in SWL. Finally, in Section 5, we summarize the results and briefly discuss directions of future work.

2. Physical model

2.1. Problem description

Cavitation inception in SWL is at least partly due to the excitation of preexisting gas nuclei by the repeated passage of the pressure pulse that is generated by the lithotripter. Though reliable measurements of the initial population of nucleation sites in vasculature is currently unavailable, bubbles are thought to exist in blood vessels under normal physiological conditions and *in vitro* experiments suggest that their population will grow with ongoing SWL treatment [5,19]. The pressure wave emitted by the lithotripter is composed of a compressive and a tensile component. During compression, which is characterized by a shockwave and a transition into tension, preexisting gas bubbles are rapidly collapsed. This shock-induced collapse is immediately followed by a period of cavitation, which is induced by the negative pressures associated with the tensile component of the lithotripter waveform. Cavitating bubbles grow to a large size and subsequently collapse. This is often referred to as a Rayleigh collapse and is driven by the static pressure difference between the bubble contents and the surrounding fluid [20]. In a typical clinical lithotripsy treatment, the pressure pluses are delivered with a frequency between 0.5 and 3 Hz. Then, as the treatment progresses, the above described bubble dynamics become cyclical and eventually more prominent and complex, with the number of nucleation sites increasing and the interaction between neighboring bubbles becoming non-negligible.

This extremely rich and varied bubble behavior poses significant modeling challenges. Specifically, the range of spatial and temporal scales that is cumulatively spanned by shock-induced collapse, Rayleigh collapse and the interaction between adjacent bubbles makes it computationally prohibitive to attempt to comprehensively simulate the bubble dynamics inside blood vessels during the lifetime of the SWL treatment. By focusing our efforts on the analysis of the shock-induced collapse of a preexisting gas bubble, inside a small blood vessel and exposed to only one lithotripter pulse, the modeling requirements imposed by the spatial and temporal scales are significantly alleviated. The spatial scales will approximately be bound by the diameter of the small blood vessels, 5 to 100 μm, while the temporal scales will be on the order of the collapse time of comparably sized bubbles, $\mathcal{O}(10)$ ns [21]. Then, the scaling arguments put forth by previous numerical studies of this nature suggest that the modeling of diffusive effects, mass transfer and surface tension, can be neglected [17,22]. Though these arguments do not strictly apply to a collapse that is confined by the presence of a blood vessel wall and the tissue that lies beyond it, it is not expected that the confinement offered by either of these two structures will be sufficient to significantly alter the scaling analysis. This assertion is partially supported by the work of Freund [21] who generalized the Rayleigh–Plesset equation of spherical bubble dynamics to gauge the potential of the blood vessel wall and the surrounding tissue to suppress bubble growth in SWL. Freund's results suggest that across a large range of experimentally measured values of the wall and tissue elasticities, as well as tissue viscosities, bubble expansion cannot be meaningfully inhibited. Though the higher reported values of tissue viscosity were shown to be more effective, we do not model viscous effects at this time. Under these circumstances, we omit modeling diffusive effects, mass

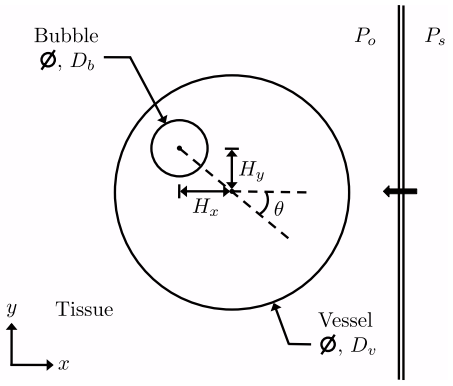

Fig. 1. Schematic of the initial condition for the shock-induced collapse of a bubble inside a deformable vessel in the x–y cross section of the 3D domain.

transfer and surface tension, and consider the bubble dynamics to be purely driven by inertia.

The most challenging part of the modeling is adequately accounting for the structure and material properties of the vessel wall and tissue. Both are anatomically complex and characterized by a non-linear mechanical response with respect to the strain and the strain rate. At strain rates associated with SWL, neither the mechanical response nor the failure criteria of the vessel wall or tissue are well understood [1]. Fortunately, since Freund's [21] analysis of the generalized Rayleigh–Plesset equation under SWL conditions suggests that bubble growth and, implicitly, wall and tissue deformation, are insensitive to a wide range of reported elastic moduli, significant modeling simplifications to the material response of these two structures can be made. Notably, we omit modeling the effects of elasticity altogether and thus avoid the implementation of complicated constitutive relationships. The resulting model of the vessel wall is an infinitely thin, flexible and non-load-bearing membrane, while the surrounding tissue, at the strain rates characteristic of SWL, is modeled as a fluid. The main drawback of this approach is that it does not allow us to characterize the potential for vascular injury in terms of stresses. Instead, we do so by reporting the maximum vessel wall pressures and deformations.

Based on our understanding of the bubble dynamics inside blood vessels, as well as our modeling approach to the behavior of the bubble, vessel wall and tissue, we idealize the initial condition for the shock-induced collapse of a bubble inside a blood vessel as schematized in Fig. 1, where an x–y cross section of an otherwise 3D domain with the regions of fluid corresponding to the bubble, vessel and tissue are identified. The initial condition consists of a spherical gas bubble, with diameter D_b, a cylindrical blood-filled vessel, or blood column, with diameter D_v, and a shockwave traveling through tissue. The bubble, positioned at $(x, y, z) = (H_x, H_y, 0)$, is located inside the vessel, which in turn is embedded in tissue and centered in the x–y plane with its axis coinciding with the z-axis. Initially, both the bubble and vessel are at atmospheric pressure, P_o, and in mechanical equilibrium. This balance is upset by the passage of the shockwave, which is illustrated in the schematic by a step increase in pressure, from P_o to P_s, with P_s set to 40 MPa so to approximate the peak positive pressure of a widely utilized clinical lithotripter, the Dornier HM3 [23]. The shockwave propagates toward the bubble and vessel in a direction that is perpendicular to the z-axis and inclined at an angle $\theta = \tan^{-1}(H_y/H_x)$ to the plane spanned by the centroid of the bubble and the axis of the vessel. Shortly after the passage of the shockwave, the bubble collapses, possibly rupturing the vessel wall and damaging the surrounding tissue. In this study, we take advantage of the geometric flexibility afforded by this initial condition to analyze the effects of vessel confinement, $1.1 \leq D_v/D_b \leq 4.0$, bubble proximity, $-0.75 \leq H_x/D_b \leq 0.75$, and shockwave angle, $0 \leq \theta \leq \pi/2$, on the potential for such injury to occur.

2.2. Equations of motion

Invoking the approximations discussed above, the shock-induced collapse of a bubble inside a blood vessel falls under the category of multicomponent flows. The latter are the subset of multiphase flows in which the component fluids are immiscible and do not change phase. In the problem under consideration, there are three fluids: the gas in the bubble, the blood in the vessel and the surrounding tissue. Each fluid is considered to be inviscid and compressible and since diffusive effects, mass transfer and surface tension are all neglected, there are no interfacial physics, *i.e.* the material interfaces are simply advected by the local velocity field. This type of multicomponent flow is then governed by the Euler system of equations, Eqs. (1)–(3), which is augmented by the advection equations for the volume fractions, Eq. (4), one for each fluid present in the flow [24].

$$\frac{\partial \rho}{\partial t} + \nabla \cdot (\rho \mathbf{u}) = 0 \tag{1}$$

$$\frac{\partial (\rho \mathbf{u})}{\partial t} + \nabla \cdot (\rho \mathbf{u} \otimes \mathbf{u} + p\mathbf{I}) = \mathbf{0} \tag{2}$$

$$\frac{\partial E}{\partial t} + \nabla \cdot ((E + p)\mathbf{u}) = 0 \tag{3}$$

$$\frac{\partial \alpha_i}{\partial t} + \mathbf{u} \cdot \nabla \alpha_i = 0, \quad i = 1, 2, 3. \tag{4}$$

In Eqs. (1)–(4), ρ is the density, $\mathbf{u} = (u, v, w)^T$ is the velocity vector in $\mathbb{R}^3$, p is the pressure, E is the total energy and α_i is the volume fraction of the ith fluid, with $0 \leq \alpha_i \leq 1$ and $\sum_{i=1}^{3} \alpha_i = 1$. The Euler system of equations holds true for each fluid in the flow and its closure is achieved by an equation of state whose character may vary with fluid identity, see Section 2.3. The advection equations for the volume fractions are used to identify the fluids and capture the material interfaces that separate them.

The governing equations of motion are non-dimensionalized in order to facilitate the analysis and interpretation of the results presented in this study. The latter are reported in a dimensionless form so to extend their applicability to the range of vessel and bubble sizes relevant to vascular injury observed in SWL. The non-dimensionalization is based on the initial bubble diameter, D_b, the density in the region of tissue processed by the shockwave, ρ_s, the pressure jump across the shockwave, $\Delta P = P_s - P_o$, and finally, a characteristic velocity based on ρ_s and ΔP, $U = \sqrt{\Delta P/\rho_s}$. The resulting non-dimensional time, position, density, velocity and pressure are given below, in Eq. (5), and denoted by an asterisk, as will all non-dimensional variables be from here on. Note that Eqs. (1)–(4) are inherently in non-dimensional form so that we omit simply rewriting them here with an asterisk for the sake of conciseness.

$$\begin{aligned} t^* &= t\frac{U}{D_b}, \qquad \mathbf{x}^* = \frac{\mathbf{x}}{D_b}, \qquad \rho^* = \frac{\rho}{\rho_s}, \\ \mathbf{u}^* &= \frac{\mathbf{u}}{U}, \qquad p^* = \frac{p}{\Delta P}. \end{aligned} \tag{5}$$

2.3. Equation of state

In order to provide closure to the Euler system of equations, it is necessary to specify the appropriate equation of state, relating the density, internal energy and pressure, for the gas in the bubble, the blood inside the vessel and the surrounding tissue. The gas in the bubble is usually a mixture of vapor and non-condensible gas, the ratio between which is dictated by the effects of mass transfer.

Table 1
Properties of air, water and 10% gelatin. These include the density, ρ, the sound speed, c, and the stiffened gas equation of state fitting parameters, γ and P_∞, which are derived from shockwave Hugoniot data [26].

Fluid	ρ (kg/m^3)	c (m/s)	γ	P_∞ (Pa)
Air	1.204	343	1.40	0
Water	1000	1450	6.12	3.43×10^8
10% Gelatin	1030	1553	6.72	3.70×10^8

Since those effects are neglected here, the bubble is assumed to be strictly composed of air, a common modeling assumption for the type of problem under consideration and one to which the jetting dynamics are not sensitive [17]. The blood and tissue are modeled by water and 10% gelatin, respectively, since water closely approximates the density and impedance of plasma and 10% gelatin those of soft tissue, like the liver and kidney [25]. Since air is expected to behave ideally and the propagation of shockwaves in both water and 10% gelatin will be a primordial feature of the flow, the stiffened gas equation of state is utilized to describe each fluid,

$$p = (\gamma - 1)\rho e - \gamma P_\infty \tag{6}$$

where e is the specific internal energy and γ and P_∞ are fitting parameters deduced from shockwave Hugoniot data. The parameters for air, water and 10% gelatin are tabulated in Table 1, along with their densities and sound speeds. Note that for air, Eq. (6) reduces to the ideal gas law with γ, the ratio of specific heats.

The appropriate values for γ and P_∞ must also be determined for those regions of the flow containing mixtures of two or more fluids. Such mixtures do not occur as a result of mixing on a molecular level, but are the product of numerical diffusion and are confined to thin regions of space neighboring material interfaces. In our simulations, material interfaces are therefore not sharp, but are diffused over a small, finite, width. For the mixture region defining a diffuse material interface, relationships for γ and P_∞ can be derived by assuming that the fluids forming the mixture are in mechanical equilibrium. This assumption ensures that the properties of a sharp material interface, *i.e.* no jump in pressure or normal velocity across it, are recovered by the diffuse material interface in the limit of infinite spatial resolution. The resulting mixture relationships for γ and P_∞ are derived by Allaire et al. [27] and reproduced here in Eqs. (7) and (8), respectively.

$$\frac{1}{\gamma - 1} = \sum_{i=1}^{3} \alpha_i \left(\frac{1}{\gamma_i - 1} \right) \tag{7}$$

$$\frac{\gamma P_\infty}{\gamma - 1} = \sum_{i=1}^{3} \alpha_i \left(\frac{\gamma_i P_{\infty,i}}{\gamma_i - 1} \right). \tag{8}$$

3. Numerical method

3.1. Spatial and temporal discretization

The numerical method originates from the work of Johnsen and Colonius [28] and has previously been utilized to study the collapse of an air bubble near a rigid wall with applications to the comminution of kidney stones in SWL [3,4,22]. It is based on a finite-volume framework with the spatial reconstruction handled by a weighted essentially non-oscillatory (WENO) scheme and the time-stepping carried out by a total-variation-diminishing (TVD) Runge–Kutta (RK) method [29,30]. The fluxes are computed with the Harten–Lax–van Leer-Contact approximate Riemann solver [31]. The resulting numerical scheme is high-order accurate in smooth regions, interface and shock-capturing, oscillation-free and lastly, discretely conserves mass, momentum and energy. Present advancements include the extension to 3D and an improved spatial reconstruction approach that is more accurate and maintains the monotonicity of the reconstructed variables [32,33].

In what follows, we used a uniform spatial and temporal discretization with a 5th order WENO reconstruction and a 3rd order TVD RK scheme. Based on a refinement study of an axisymmetric shock-induced collapse, a spatial resolution of 100 cells per bubble diameter was selected for each simulation and the time-step was chosen so to keep the Courant–Friedrichs–Lewy number below 0.2 to ensure numerical stability. Due to the resulting computational cost, the numerical scheme was parallelized and each simulation was performed on a parallel system, on 3456 compute cores with a run-time between one and two days.

3.2. Non-reflecting boundary conditions

In the idealized initial condition of the shock-induced collapse of a gas bubble in a blood vessel, the length of the vessel and the thickness of the surrounding tissue are both considered to be large compared to the bubble and vessel diameters. The resulting free-space problem is approximated in the simulations by truncating the length of the vessel to $5D_b$, the thickness of the buffer of tissue, in each coordinate direction perpendicular to the axis of the vessel, to $2D_b$ and applying the non-reflecting boundary conditions of Thompson [34,35]. The performance of these boundary conditions can be assessed by ensuring that the computational domain that is simulated is large enough, *i.e.* that an increase in the simulated vessel length and/or tissue thickness does not result in large variations of the measured vessel wall pressures and/or deformations. In our experience, the non-reflecting boundary conditions perform well, as doubling the simulated vessel length and/or tissue thickness results in less than a 5% change in both the maximum vessel wall pressure and deformation.

4. Results and discussion

In this section, the results of the parametric study are analyzed. The ensuing observations are cast in the context of clinical SWL or more precisely, the potential for vascular damage to occur therein. We start by discussing the dynamics characterizing the shock-vessel–bubble system for the case with the highest potential for injury. This is the case with the highest vessel confinement and consequently the largest recorded vessel wall pressure and deformation. Since this geometric configuration is anticipated to result in the strongest coupling between the bubble and the vessel, the time history of various variables aimed at characterizing this interaction is presented. For the bubble, these metrics include the volume, the centroid location and the jet velocity, while for the vessel, they include the wall pressure and deformation. Lastly, following the analysis of this specific case, the results of the parametric study of the vessel confinement, Section 4.2, bubble proximity, Section 4.3, and shockwave angle, Section 4.4, are presented, with a focus on the effect of each parameter on the potential for vascular injury to occur.

4.1. Overview of shock-vessel–bubble interaction

The coupled dynamics of the shock-vessel–bubble system can best be understood by analyzing the scenario in which the volumetric confinement of the bubble, as exacted by the vessel, is most restrictive. It is in this particular case, where $(D_v^*, H_x^*, \theta) = (1.1, 0, 0)$, that the vessel wall pressures and deformations are highest. Figs. 2 and 3 document the shock-vessel–bubble interaction for this geometric configuration with time snapshots of notable instants of the shock-induced collapse. In Fig. 2, the deformations of the bubble and vessel wall are rendered by

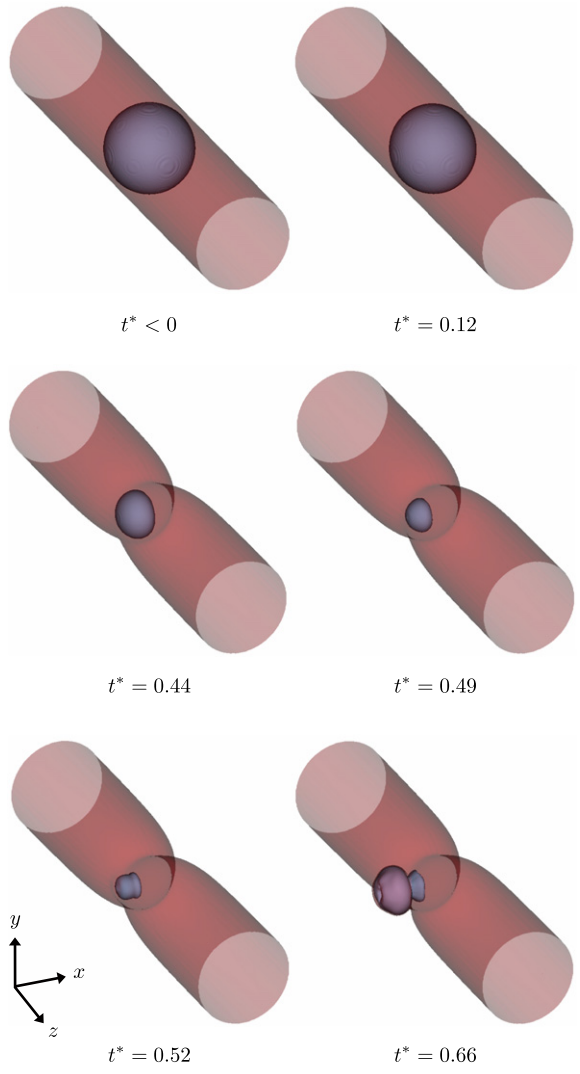

Fig. 2. Time snapshots of the deformation of the bubble and the vessel wall for $(D_v^*, H_x^*, \theta) = (1.1, 0, 0)$. The bubble is depicted by the 0.5 isosurface of the volume fraction of air and the vessel wall by the one of 10% gelatin.

isosurfaces of air and 10% gelatin, respectively, while in Fig. 3, the interactions between different waves and material interfaces in the x–z plane are illustrated by the pressure and velocity fields. The dynamics of the shock-vessel–bubble system are initiated as the left-moving shockwave, originally traveling in 10% gelatin, or tissue, for $t^* < 0$, is transmitted through the cylindrical water column, or vessel, and impacts the air bubble at $t^* = 0$. Since the impedance mismatch between 10% gelatin and water is small, but that between water and air is large, the shockwave is predominantly transmitted through the vessel but only partly so through the bubble, against which it also reflects and diffracts in the form of an expansion wave. At $t^* = 0.12$, the shockwave has almost fully traversed the vessel but, due to the significantly lower sound speed in air compared to water, has only began to transmit through the bubble. This difference in sounds speeds induces the proximal interface of the bubble, *i.e.* the side originally closest to the shockwave, to collapse first, invaginating the proximal wall of the vessel along the way. By $t^* = 0.44$, the shockwave has long left the domain and as a result, the distal interface of the bubble has also begun to collapse, invaginating the distal wall of the vessel. As the collapse progresses, the bubble continues to shrink and in addition, translates in the direction of the propagation of the shockwave. The latter effect enhances the invagination of the proximal wall of the vessel, while discouraging that of the distal,

Table 2
The minimum bubble volume, V_{min}^*, x-coordinate of the centroid, $\bar{x}_{min}^*$, and proximal interface velocities, $u_{p,min}^*$ and $u_{p,min}$, for $(D_v^*, H_x^*, \theta) = (1.1, 0, 0)$ and $(D_v^*, H_x^*, \theta) = (4.0, 0, 0)$.

D_v^*	V_{min}^*	$\bar{x}_{min}^*$	$u_{p,min}^*$	$\lvert u_{p,min}\rvert$ (m/s)
1.1	2.19×10^{-2}	-5.98×10^{-1}	−5.43	1061
4.0	2.30×10^{-2}	-6.02×10^{-1}	−5.04	985

which at $t^* = 0.49$ has reached its maximum. From here on, the bubble begins to directly interact with the proximal vessel wall, pushing it outward as it translates. The translation of the bubble is accelerated by the formation of the liquid jet, the presence of which is already evident in this snapshot, but far more pronounced at $t^* = 0.52$, when the minimum bubble volume is achieved. As the liquid jet forms, it impacts the distal bubble interface and vessel wall producing a strong water-hammer shockwave in the process. The latter propagates spherically from the point of origin, generating large pressures on both the proximal and distal vessel walls. Shortly after the water-hammer shockwave is emitted, the maximum invagination of the proximal vessel wall is achieved, while the distal vessel wall begins to distend, pushed outward by the force of the liquid jet. The final moments of the shock-vessel–bubble interaction, as simulated in this study, are captured at $t^* = 0.66$ and characterized by the continued distention of the distal vessel wall by a bubble that is now shaped like a vortex ring. At this instant in time, the water-hammer shockwave is also still visible, propagating outward, near the outskirts of the domain.

To better understand how the bubble dynamics are influenced by the presence of the vessel, the time history of various bubble metrics is charted in Fig. 4. The metrics include the bubble volume, V^*, x-coordinate of the centroid, $\bar{x}^*$, and distal and proximal interface velocities, u_d^* and u_p^*, respectively, the latter of which the measurement locations are annotated on the contour of the bubble in the x–z plane, in the schematic of Fig. 5(a). The dynamics of the bubble are initially excited by the impact of the shockwave on its proximal interface, an event that is denoted by the sudden jump in the corresponding velocity. As this velocity grows in time, the proximal interface involutes, inducing the volume occupied by the bubble to slowly shrink and its centroid to begin traveling in the direction of the propagation of the shockwave. At $t^* = 0.16$, the passing shockwave has completed processing the bubble so that its distal interface has also begun to involute. As the collapse of the bubble progresses, the pace accelerates, peaking shortly before the minimum bubble volume is reached. The minimum volume, $V^* = 2.19 \times 10^{-2}$, occurs at $t^* = 0.52$ and marks the end of the collapse phase. The liquid jet reaches its largest velocity, $u_p^* = -5.43$, at $t^* = 0.50$. As the liquid jet nears the distal bubble interface, it begins to notably slow down, with the ensuing collision preceding the occurrence of the minimum volume. The formation and impact of the liquid jet leads both the distal and proximal bubble interfaces to travel in the direction of the propagation of the shockwave. Since the velocity of the proximal interface is larger, it eventually coalesces with the distal interface and the bubble forms a vortex ring at $t^* = 0.64$. In the final moments of the simulation, the bubble is in its rebound phase and so as its centroid continues to travel in the direction of the propagation of the shockwave, its volume slowly increases.

The extrema of the bubble metrics plotted in Fig. 4 for $D_v^* = 1.1$ are contrasted in Table 2 with those for $D_v^* = 4.0$, a nearly four-fold difference in the diameter of the vessel that ensures that in the latter case the bubble negligibly interacts with the vessel walls. In Table 2, the minimum bubble volume, x-coordinate of the centroid and proximal interface velocity are listed. For both diameters, the values of these bubble metrics at $t^* = 0$ are $V^* = 1$, $\bar{x}^* = 0$ and $u_p^* = 0$, so that the minima represent a significant deviation from the initial values. Table 2 indicates that the impact

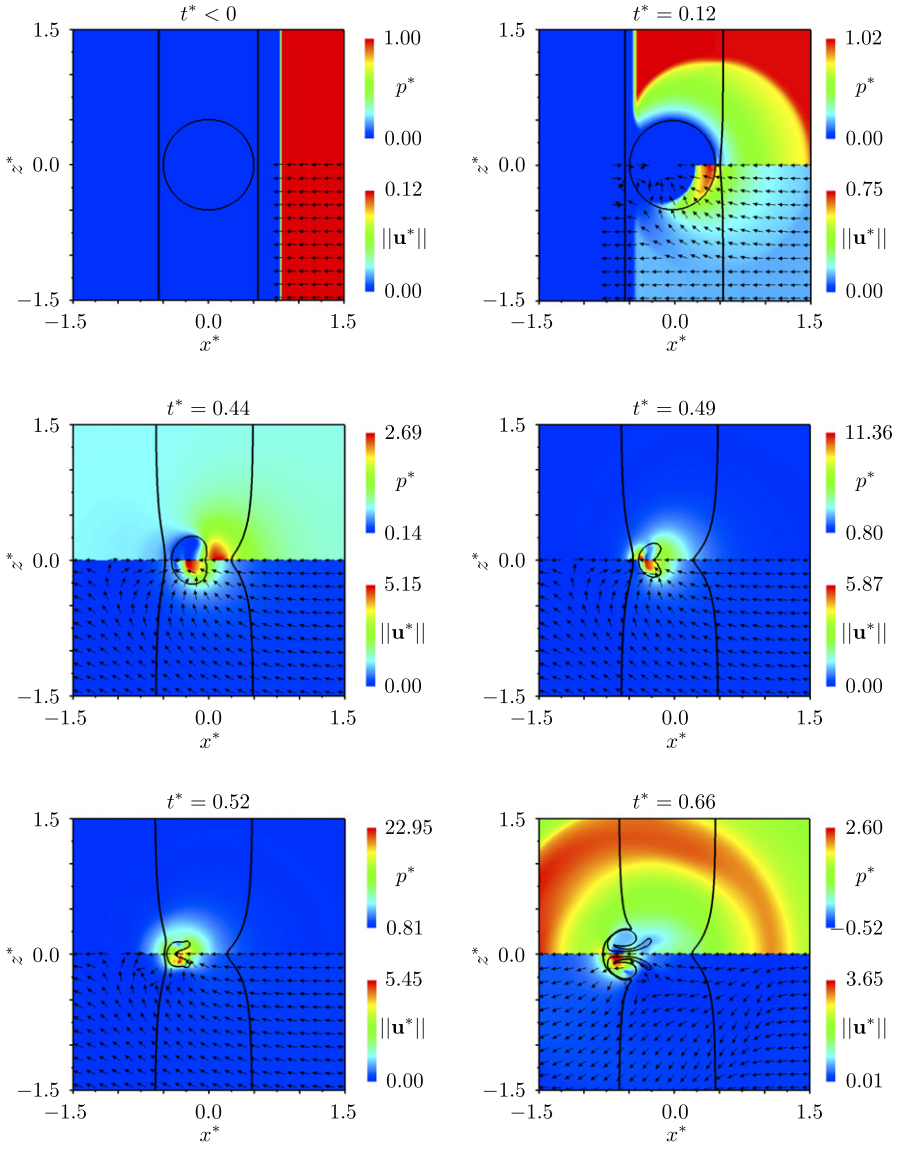

Fig. 3. Time snapshots of the flooded pressure contours (p^*, upper panel half), the flooded velocity magnitude contours ($\|\mathbf{u}^*\|$, lower panel half) and the velocity vector field ($\mathbf{u}^*$, lower panel half) in the x–z cross section of the 3D domain for $(D_v^*, H_x^*, \theta) = (1.1, 0, 0)$. For clarity, isocontours of the volume fractions of air and 10% gelatin are included as in Fig. 2.

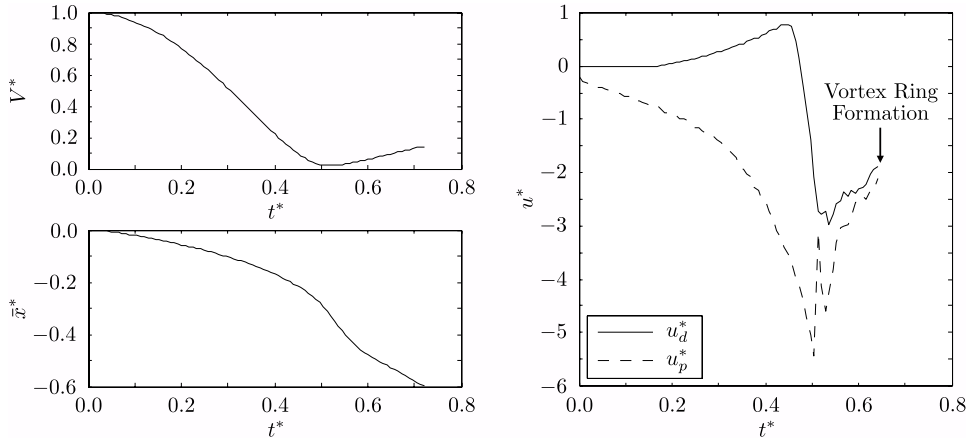

Fig. 4. Time history of the bubble volume ($V^* = V/V_{t^*=0}$, top left), x-coordinate of the centroid ($\bar{x}^*$, bottom left) and distal and proximal interface velocities (u_d^* and u_p^*, right) for $(D_v^*, H_x^*, \theta) = (1.1, 0, 0)$. Note that a schematic of the measurement locations of u_d^* and u_p^* may be found in Fig. 5(a).

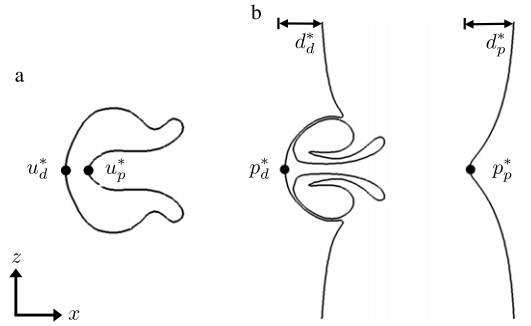

Fig. 5. Schematic of the measurement locations of various bubble and vessel wall metrics in the x–z cross section of the 3D domain for $\theta = 0$. In (a), the contour of the bubble is utilized to indicate the probe locations for the distal and proximal bubble interface velocities (u_d^* and u_p^*). In (b), the contour of the vessel wall, in addition to that of the bubble, is drawn to illustrate the probe locations for the distal and proximal vessel wall pressures (p_d^* and p_p^*) and deformations (d_d^* and d_p^*).

of the vessel walls on the dynamics of the bubble are marginal. In fact, for the almost fourfold increase in the diameter of the vessel, between the largest and the smallest vessel confinement, the percent change in any one of the minima does not exceed 7%. Nevertheless, the collapse is somewhat stronger when the vessel walls are closer to the bubble, as suggested by the smaller bubble volume and larger liquid jet velocity that are achieved in this case. It is likely that this is primarily due to the internal reflections of the primary shockwave inside the vessel, which additionally process the bubble and induce a stronger collapse. This mechanism would play a less prominent role in the case of a smaller vessel confinement since the shockwaves reflected inside the vessel would have to travel farther to once again process the bubble. The analogous mechanism is reported by Johnsen [22] for the shock-induced collapse of a bubble near a rigid wall. The data in Table 2 is consistent with previous findings and indicates that overall the vessel has a very limited influence on the behavior of the bubble [21]. Since the properties of 10% gelatin are similar to those of water, see Table 1, this is not all that surprising and ultimately suggests that from the point of view of the bubble, the shock-induced collapse inside a vessel can adequately be approximated to that in a free field. The maximum liquid jet speeds for $D_b^* = 1.1$ and 4.0 are also listed in Table 2 and agree well with the expected free field values, around 1000 m/s [22,36].

Seeing that the collapse of the bubble is insensitive to the presence of the vessel, from this point forward, the study focuses on the reverse coupling. In Fig. 6, the latter is explored through the time history of the distal and proximal vessel wall pressures, p_d^* and p_p^*, and deformations, d_d^* and d_p^*. The measurement locations of these metrics are annotated on the contour of the vessel wall in the x–z plane, in the schematic of Fig. 5(b), and are selected based on the expected locations of the vessel wall pressure and deformation extrema. In Fig. 6, the influence of the dynamics of the bubble onto those of the vessel is evident almost immediately after the impact of the primary shockwave on the proximal bubble interface. The latter, at $t^* = 0$, marks the beginning of the involution of that side of the bubble, which nearly simultaneously drives the invagination of the proximal vessel wall. The invagination of the distal vessel wall follows soon thereafter, around $t^* = 0.16$, when the shockwave has completed processing the entire bubble and the distal bubble interface involutes. In both cases, the invagination is due to the sink flow produced by the volumetric contraction of the bubble, which persists until the end of the collapse phase, at $t^* = 0.52$. Note, however, that the largest invagination of the distal vessel wall, $d_d^* = -0.13$, is achieved before the end of the collapse phase, at $t^* = 0.49$, while that of the proximal vessel wall, $d_p^* = -0.28$, is achieved afterward, at $t^* = 0.54$. This is attributable to the translation of the bubble, which, as the collapse progresses, moves away from the proximal vessel wall and closer to the distal wall. This is also the primary reason why the proximal vessel wall invaginates more than the distal one and ultimately, why the invagination of the latter is arrested shortly before the end of the collapse phase. Once the invagination of the vessel is complete, the remaining deformations are primarily due to the jetting of the bubble. The liquid jet impacts the distal bubble interface and vessel wall, almost simultaneously, at $t^* = 0.51$, and generates a water-hammer shockwave. This impact is immediately followed by a sustained decrease in the invagination of the distal vessel wall and a tremendous spike in its pressure, which peaks at $t^* = 0.53$ with $p_d^* = 11.04$ and is due to the passage of the water-hammer shockwave. The proximal vessel wall remains largely unaffected by these events, only experiencing a slight reduction in its invagination when the water-hammer shockwave finally reaches it. This occurs at $t^* = 0.56$ and corresponds to the brief increase in the proximal vessel wall pressure, which peaks at $p_p^* = 4.46$. From here on, since dissipative and elastic effects are neglected, the distal vessel wall continues to deform under the forcing of the liquid jet, while the proximal one remains invaginated. As such, the last moments of the simulation are characterized by the distention of the distal vessel wall, which is first achieved at $t^* = 0.57$ and further simulated until $t^* = 0.72$, when $d_d^* = 0.26$.

In order to put into perspective the potential for vascular injury associated with the above discussed vessel wall pressures and deformations, it is instructive to consider a specific physical

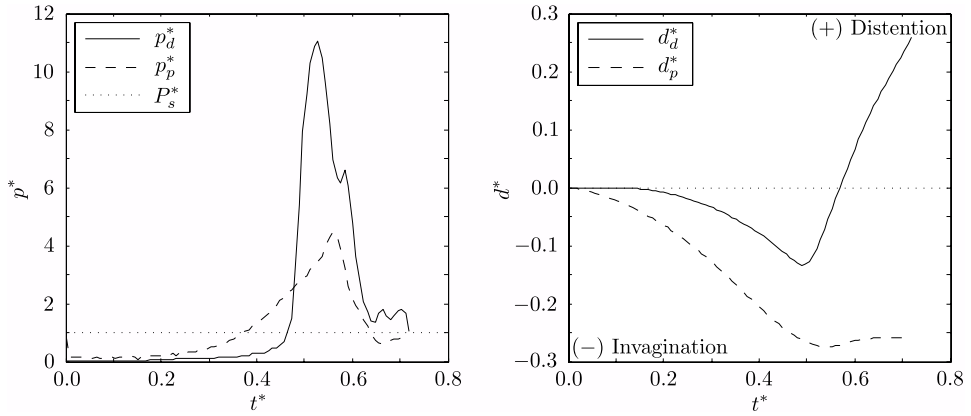

Fig. 6. Time history of the distal and proximal vessel wall pressures (p_d^* and p_p^*, left) and deformations (d_d^* and d_p^*, right) for $(D_v^*, H_x^*, \theta) = (1.1, 0, 0)$. Note that the pressure associated with the initial shockwave, P_s^*, is plotted against p_d^* and p_p^* to illustrate the ability of the shock-induced collapse to amplify the strength of the primary shockwave. For a schematic of the measurement locations of p_d^*, p_p^*, d_d^* and d_p^* please refer to Fig. 5(b).

Table 3
A comparison between experiment and simulation of the largest distal and proximal wall invaginations and distentions of a $D_v = 22$ μm blood vessel. These are characterized by the deformation distance, d, and an approximation of the largest strain along the direction of this deformation based on small strain theory, $-d/R_v$, where R_v is the radius of the undeformed vessel. The experimental data is from Chen et al. [9], for a blood vessel in rat mesentery axisymmetrically deformed by ultrasonic cavitation, while the simulation data is from $(D_v^*, H_x^*, \theta) = (1.1, 0, 0)$. For a schematic of the measurement locations of d please refer to Fig. 5(b), where the distal and proximal vessel wall deformations correspond to d_d^* and d_p^*, respectively.

Vessel wall	Experiment		Simulation	
	d (μm)	$-d/R_v$ (%)	d (μm)	$-d/R_v$ (%)
Distal				
Invagination	−7	60	−2.68	24.32
Distention	3	−30	5.18	−47.08
Proximal				
Invagination	−7	60	−5.50	50.01
Distention	3	−30	0.00	0.00

geometry in dimensional form. To do so, the geometric configuration is adapted from a relevant test case considered in the experimental work of Chen et al. [9], who studied the deformations of blood vessels in rat mesentery by ultrasonic cavitation on a microsecond time scale. The referenced test case consists of a lipid-coated perfluoropropane microbubble growing and collapsing inside a $D_v = 22$ μm saline-filled blood vessel due to the passage of an ultrasound pressure pulse. The sinusoidal characteristics of this incident pressure wave contrast drastically with the step increase in pressure that epitomizes a shockwave so that the interactions between the bubble and the vessel in the experiment differ categorically from those observed in the simulation. Nevertheless, the magnitude of the largest measured deformations between the experiment and the simulation are comparable and thus provide a meaningful way by which observations regarding the potential for vascular injury in shock-induced collapse can be made. Then, the results of the simulation are dimensionalized based on the diameter of the blood vessel in the experiment and the jump in pressure across the shockwave in the simulation. The former helps determine the characteristic length scale, *i.e.* the initial bubble diameter, $D_b = 20$ μm, and allows for the dimensionalization of the vessel wall deformations, while the latter is the characteristic pressure scale, $\Delta P = 399$ MPa, and enables the dimensionalization of the vessel wall pressures.

In Table 3, the largest distal and proximal vessel wall invaginations and distentions are compared between the experiment and the simulation. They are characterized by the deformation distance, d, and an approximation of the largest strain along the direction of this deformation derived from small strain theory, $-d/R_v$, where R_v is the radius of the undeformed vessel. Note that $-d/R_v$ corresponds to the largest principal radial strain at the wall of a cylindrical hole in an infinite medium, as obtained from the plane strain solution of the linear elasticity equations. Since the strains in the experiment and the simulation are large and the associated state of strain is multiaxial, this approximation is crude, but, as shall be demonstrated in Section 4.2, is also likely to be conservative. The estimated values of the strains suggest that both in the experiment and in the simulation the likelihood of vascular injury is high. Uniaxial tension and compression experiments, though not strictly foretelling of material response under multiaxial loading, indicate that the strains documented in Table 3 near, if not exceed, measurements based on large strain theory of the ultimate strains of most soft tissues. This is the case for the human liver parenchyma, which has an ultimate Green–Lagrange strain of about 24% in tension and −35% in compression, as well as the porcine kidney cortex and capsule, which are acceptable human test surrogates and have tensile and compressive ultimate strains that are comparable to those mentioned for the liver [37–40]. Despite the high potential for vascular injury, however, there is no evidence provided by the experiment of Chen et al. that suggests that any permanent damage is sustained by the blood vessel due to these large deformations. In fact, it appears that once the bubble dynamics degenerate, the blood vessel returns to its undeformed configuration on a millisecond time scale. Though this does not preclude the possibility of vascular injury altogether, it does potentially restrict its extent and suggests that at most, it is sufficiently localized and/or scarce such that the undeformed state of the vessel may still be recovered.

For the geometric configuration currently under consideration, however, it is probable that the potential for injury in the simulation is greater than that in the experiment. Albeit the deformations of the vessel are moderately larger in the latter, the shock-induced collapse in the simulation is driven by pressures that are an order of magnitude higher than those of ultrasonic cavitation in the experiment. Not only does this insinuate that the resulting vessel wall pressures are also likely to be more prominent but, based on the measured collapse times of the bubble, 53.25 ns in the simulation and approximately 1 μs in the experiment, it also results in faster strain rates, $\mathcal{O}(10^7)$ compared to $\mathcal{O}(10^5)$ s^{-1}, which, in soft tissue, are associated with lower ultimate strains [37–40]. Note that in general, faster strain rates also imply larger failure stresses. However, the maximum distal and proximal vessel wall pressures recorded in the simulation, $p_{d,max} = 440$ MPa and $p_{p,max} = 178$ MPa, despite being transient, are at least an order of magnitude higher than the failure stresses that would be expected in soft tissue [37–40].

4.2. Effects of vessel confinement

Recall that in SWL, the onset of vascular injury is predominantly limited to small blood vessels, such as capillaries, arterioles and venules [1,6,7]. This suggests that the level of volumetric confinement of the bubble dynamics within a particular vessel may play a significant role in determining whether the latter is damaged or not during treatment. Then, to characterize the potential for vascular injury as a function of the vessel confinement, the vessel diameter is parametrically varied, $1.1 \leq D_v^* \leq 4.0$, with the remaining aspects of the geometry of the problem held fixed, $(H_x^*, \theta) = (0, 0)$. The resulting extrema of the distal and proximal vessel wall pressures and deformations are plotted in Fig. 7 and show a strong direct relationship between the strength of the volumetric confinement of the bubble and the potential for injury of the vessel. In other words, for the shock-induced collapse of a fixed-size bubble, centered inside a vessel, an increase in the diameter of the vessel brings about a decrease in the extrema of the distal and proximal vessel wall pressures and deformations and thus inherently, a decrease in the potential for vascular injury. The relationship between the vessel diameter and its wall pressure is readily fitted by a power law, Eq. (9), while the analogous relationship for the wall invagination closely adheres to the potential theory of a sink flow, Eq. (10).[2]

$$p_{max}^*\left(D_v^*\right) = \frac{A}{D_v^* + 2\bar{x}_c^*} + B \tag{9}$$

$$d_{min}^*\left(D_v^*\right) = \frac{1}{2}\left[\left(D_v^{*3} + C\right)^{\frac{1}{3}} - D_v^*\right]. \tag{10}$$

In Eqs. (9) and (10), A, B and C are the fitting parameters and $\bar{x}_c^*$ is the x-coordinate of the centroid of the bubble at the end of the

[2] This equation may be derived by assuming a 3D sink flow at the initial position of the bubble, described by the velocity potential $\phi(r) = -\frac{m}{4\pi r}$, where m is the sink strength and r is the radial distance from its origin, and evaluating the induced displacements at the position of the vessel walls along the x-axis.

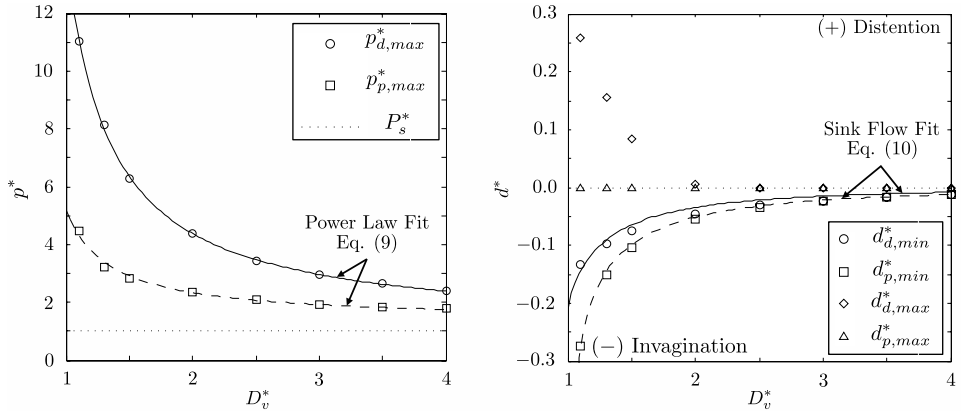

Fig. 7. Effects of vessel confinement, D_v^*, on the extrema of the distal and proximal vessel wall pressures (p_d^* and p_p^*, left) and deformations (d_d^* and d_p^*, right) for $(H_x^*, \theta) = (0, 0)$. Note that the pressure associated with the initial shockwave, P_s^*, is plotted against p_d^* and p_p^* to illustrate the ability of the shock-induced collapse to amplify the strength of the primary shockwave. For a schematic of the measurement locations of p_d^*, p_p^*, d_d^* and d_p^* please refer to Fig. 5(b).

Table 4
Effects of vessel confinement, D_v^*, for $(H_x^*, \theta) = (0, 0)$, on the extrema of the distal and proximal Green–Lagrange strains, E_d and E_p, in the tissue surrounding the vessel. The strains are computed in the direction of the distal and proximal vessel wall deformations, d_d^* and d_p^*, along the x-axis, with their extrema invariably occurring at the vessel walls. For a schematic of the measurement locations of d_d^* and d_p^* please refer to Fig. 5(b).

D_v^*	$E_{d,min}$ (%)	$E_{d,max}$ (%)	$E_{p,max}$ (%)
1.1	−49.96	120.03	778.94
1.3	−46.10	41.40	87.64
1.5	−26.72	21.70	38.14
2.0	−1.86	7.54	11.72
2.5	0.00	3.63	5.46
3.0	0.00	2.04	3.04
3.5	0.00	1.27	1.88
4.0	0.00	0.85	1.24

collapse phase, which, nearly independently of the diameter of the vessel, is equal to 0.33. For the distal vessel wall, the fitting parameters are given by $A = 2.25$, $B = 1.05$ and $C = -0.80$, while those for the proximal vessel wall are given by $A = 0.66$, $B = 1.36$ and $C = -1.17$. Note that the power law is typically used to correctly model the relationship between the maximum pressure experienced at a rigid planar wall and the distance of the latter away from a bubble at collapse [3,4,18,22]. It fits the pressure data well, however, despite the compliance and displacement of the distal and proximal vessel walls. The sink flow model also constitutes a good fit to the invagination data, regardless of the displacement of the bubble and the asymmetry of its collapse.

Based on the vessel wall pressure and deformation data presented in Fig. 7, it is obvious that the potential for vascular injury decays rapidly with a decreasing confinement of the bubble by the vessel. It still remains unclear, however, whether any vascular injury is sustained at even the highest level of confinement considered, $D_v^* = 1.1$, see Section 4.1, and if so, whether a threshold exists such that increasing the diameter of the vessel beyond it results in a vanishing potential for its damage to occur. To attempt to answer these two questions, it is useful to reinterpret the relationship between the deformation of a vessel wall and the initial diameter of the vessel, as one between the displacement of a fluid element and its initial position. This new viewpoint requires that the water and 10% gelatin be thought of as a single fluid and that the extrema of the vessel wall deformations occur at the same instant in time across the different vessel diameters. The former requirement is approximately satisfied as a result of the similarity between the properties of water and 10% gelatin, see Table 1, while the latter one may easily be verified to roughly hold true and is evidenced by the excellent goodness-of-fit of the sink flow model which relies on the same premise. Then, based on the reinterpretation of the relationship between the deformation of a vessel wall and the initial diameter of the vessel, the corresponding data in Fig. 7 may alternatively be understood to describe temporal snapshots of the displacements of fluid elements at distal and proximal locations with respect to the bubble, as a function of their initial position and for the shock-induced collapse in a free field. The resulting implication is that the normal finite strain along the direction of the displacements of the fluid elements may readily be determined in the free field surrounding the bubble based on the slope of the displacements versus initial position. In other words, the Green–Lagrange strain in the x-direction and along the x-axis may be obtained in the tissue surrounding the vessel from the slope of the invaginations and distentions versus initial diameter. For the invagination data, the slope is computed from the derivative of the fitted sink flow model, while for the distention data, it is evaluated by a piecewise linear approximation. The extrema of the strain are tabulated as a function of the vessel diameter in Table 4, where $E_{d,max}$ and $E_{p,max}$ correspond to the largest tensile tissue strains on the distal and proximal sides of the vessel, due to invagination, while $E_{d,min}$ is the largest compressive tissue strain on the distal side of the vessel, due to distention, and $E_{p,min}$ is not included in the table since the proximal vessel wall does not distend. For all of the vessel diameters considered in this confinement study, both the largest tensile and compressive tissue strains are invariably located at the wall of the vessel, rather than further within the tissue, and are reported in the table using Eqs. (11) and (12), respectively, which are obtained by evaluating the normal component of the Green–Lagrange strain tensor at the vessel wall.

$$E_{max}\left(D_v^*\right) = 2d_{min}^{*\prime}\left(D_v^*\right) + \frac{1}{2}\left[2d_{min}^{*\prime}\left(D_v^*\right)\right]^2 \tag{11}$$

$$E_{min}\left(D_v^*\right) = 2d_{max}^{*\prime}\left(D_v^*\right) + \frac{1}{2}\left[2d_{max}^{*\prime}\left(D_v^*\right)\right]^2. \tag{12}$$

Note that in Eqs. (11) and (12), the factor of two multiplying the derivatives of the vessel wall invaginations and distentions is necessary since these are given as a function of the vessel diameter rather than its radius. As anticipated, the documented vessel wall strains are substantial for the highest levels of confinement, but do drop off rapidly as the latter is decreased. Based on the uniaxial tensile and compressive tissue experiments discussed in Section 4.1 [37–40], it seems probable that for $D_v^* = 1.1$ and 1.3, both the distal and proximal vessel walls are injured in invagination, due to tensile failure, while only the distal vessel wall is at risk in distention, due to compressive failure. Beyond $D_v^* = 1.3$, however, the potential for either of these two mechanisms

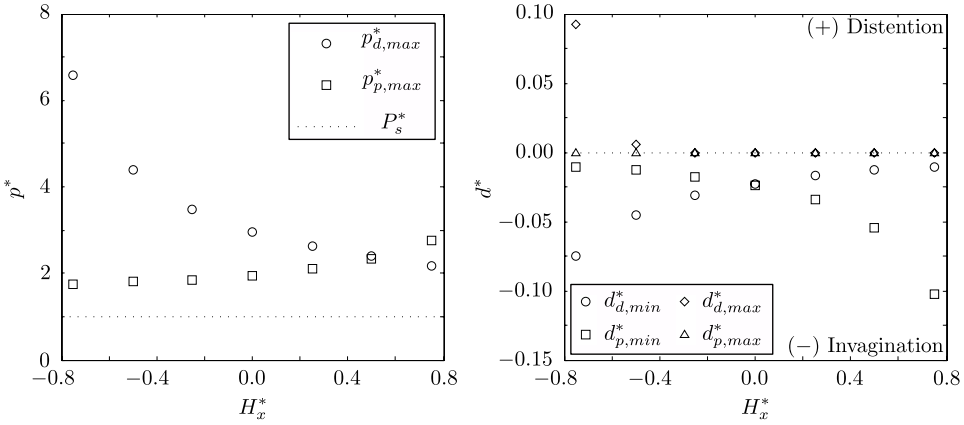

Fig. 8. Effects of bubble proximity, H^*_x, on the extrema of the distal and proximal vessel wall pressures (p^*_d and p^*_p, left) and deformations (d^*_d and d^*_p, right) for $(D^*_v, \theta) = (3, 0)$. Note that the pressure associated with the initial shockwave, P^*_s, is plotted against p^*_d and p^*_p to illustrate the ability of the shock-induced collapse to amplify the strength of the primary shockwave. For a schematic of the measurement locations of p^*_d, p^*_p, d^*_d and d^*_p please refer to Fig. 5(b).

to inflict much damage is limited, with injury due to distention, *i.e.* the impact of the liquid jet, presumably ruled out for $D^*_v \geq 1.5$ and injury due to invagination, *i.e.* the decrease in the bubble volume, unlikely to be a factor for $D^*_v \geq 2.0$. Of course, since information regarding the strains has been limited to the x-axis, extracted from a single instant in time and benchmarked against uniaxial, rather than multiaxial, loading experiments of tissue, the above thresholds are most likely rough estimates. These shortcomings will be addressed in the future by resolving the 3D, time-dependent, strain field and comparing it more relevant experimental data for tissue, as it becomes available.

4.3. Effects of bubble proximity

The effects of the proximity of the bubble to the distal and proximal vessel walls are parametrically investigated by varying the initial location of the bubble inside the vessel, along the x-axis, $-0.75 \leq H^*_x \leq 0.75$, while maintaining the remaining aspects of the geometry of the problem fixed, $(D^*_v, \theta) = (3, 0)$. The results are plotted in Fig. 8 and illustrate the relationships between the proximity of the bubble to the distal and proximal vessel walls and the extrema of the measured vessel wall pressures and deformations. These relationships confirm, as one would already anticipate, that the extrema of the pressures and deformations at a particular vessel wall increase in magnitude with a decreasing stand-off distance of the initial position of the bubble, while the opposite is true when the stand-off distance increases. Naturally, the associated potential for vessel wall injury is expected to obey the exact same trend so that, as a result, an optimization problem regarding the minimization of the cumulative damage to the distal and proximal vessel walls arises with respect to the initial stand-off distance of the bubble from each side of the vessel. From Fig. 8, the solution to the problem is evident and may be read off of the plot of the deformation data which indicates that when the bubble is approximately centered, the extrema of the distal and proximal vessel wall deformations are collectively lowest. This result is expected to be sensitive to the vessel to bubble diameter ratio and so, as part of future work, it may be instructive to perform a bubble proximity parametric study with respect to several of its values. This study would also address the complementary maximization problem, the solution to which identifies the position of a bubble within a vessel that leads to the largest cumulative damage. Ultimately, however, it would allow us to pinpoint the position and size of the smallest bubble, within a particular vessel, for which the shock-induced collapse induces sufficient vascular deformations to cause injury.

4.4. Effects of shockwave angle

The angle at which the shockwave impacts the blood vessel, as well as the bubble inside it, is likely to play a considerable role in the assessment of the potential for vascular injury due to shock-induced collapse in SWL. Thus, as a first step, this study examines the range of incident shockwave angles defined by $0 \leq \theta \leq \pi/2$, in an otherwise fixed geometric configuration, where $D^*_v = 3.0$ and $H^{*2}_x + H^{*2}_y = 0.75^2$. More precisely, four discrete shockwave angle values are considered; $\theta = 0, \pi/6, \pi/3$, and $\pi/2$, and their effect on the potential for vascular injury is evaluated by measuring the resulting extrema of the pressures and deformations at the vessel wall. Note that at this time, the convention regarding the distal and proximal vessel walls is no longer practical, so that the extrema of the measured wall pressures and deformations are simply denoted by p^*_{max}, d^*_{min} and d^*_{max}, and are reported where they are the highest, which is usually in the vicinity of the location at which the bubble collapses. The results of this parametric study confirm that the shockwave angle plays a substantial role in determining whether a vessel wall nearby a collapsing bubble sustains any damage. This is supported by the sharp decrease in the maximum pressure and distention, associated with the impact of the liquid jet, that results from an increase of the angle of incidence of the shockwave from $\theta = 0$ to $\pi/2$. Recall that at $\theta = 0$, the liquid jet is directly aimed at the vessel wall and is therefore optimally oriented to induce injury, generating both a large vessel wall pressure, $p^*_{max} = 6.57$, and distention, $d^*_{max} = 9.27 \times 10^{-2}$. However, at $\theta = \pi/2$, the angle of incidence of the shockwave is such that the generated liquid jet predominantly travels alongside the curvature of the vessel, with the tip of the jet farther away from the closest vessel surface, which results in a significantly reduced vessel wall pressure, $p^*_{max} = 3.85$, and no distention. The maximum invagination of the vessel wall, on the other hand, associated with the decrease in the bubble volume, is far better sustained as a function of the shockwave angle, with $d^*_{min} = -7.45 \times 10^{-2}$ at $\theta = 0$ and $d^*_{min} = -8.97 \times 10^{-2}$ at $\theta = \pi/2$. This is not wholly unexpected since the sink flow which causes the invagination, though asymmetric, does act in all directions and is bound to be more insensitive to the angle of the shockwave than the liquid jet is.

5. Conclusions

Motivated by the possible link between the shock-induced collapse of preexisting gas nuclei and the onset of vascular injury in SWL, we have undertaken a first step toward characterizing the relevant shock-vessel–bubble interactions and evaluating

their potential to result in vascular deformations in excess of the thresholds necessary for onset of damage. Specifically, we considered the asymmetric shock-induced collapse of an air bubble, immersed in a cylindrical water column and embedded in 10% gelatin. As part of the parameter space, the vessel to bubble diameter ratio, D_v^*, the x-coordinate of the bubble within the vessel, H_x^*, and the angle at which the shockwave impacts the bubble and vessel, θ, were investigated. The results were analyzed in the context of the likelihood of vascular injury to have occurred and the identity of the mechanism that may have initiated it. The present results suggest that the invagination of the vessel, due to the volumetric compression of the bubble, and its subsequent distention, instigated by the impact of the liquid jet, are the primary mechanisms by which a vessel might be damaged, with the potential for injury at its peak when the volumetric confinement of the bubble is highest, the bubble is nearest the vessel wall and/or the angle of incidence of the shockwave is such that the distance between the jet tip and the nearest vessel surface is minimized. For a particular case considered, the 40 MPa shockwave utilized in this study to collapse the bubble generated a vessel wall pressure of almost 450 MPa and produced both an invagination and distention of nearly 50% of the initial vessel radius.

Our observations regarding the potential for vascular injury based on the derived Green–Lagrange strains should be interpreted with caution, since strong conclusions regarding injury are difficult to make when the state of stress and strain in the simulations is multiaxial and the results of only uniaxial tensile and compressive experiments of tissue are available for comparison. As part of our future work, we intend to resolve the 3D, time-dependent, strain field, by tracking massless particles throughout the flow, and extend the tissue model by accounting for the effects of viscosity and ultimately elasticity. This should improve the predictive capabilities of the utilized physical model and as histological data of vascular injury becomes available, provide a more compelling means to compare simulation and experiment.

Acknowledgments

We are thankful for the valuable conversations with the other members of the Program Project Grant group, which is supported by the National Institutes of Health under grant PO1-DK043881. In particular, discussions with Drs Michael Bailey, Jonathan Freund, Wayne Kreider, Thomas Matula and Oleg Sapozhnikov were extremely helpful. In addition, we would also like to thank Drs Luigi Perotti and Ivan Vlahinic for their invaluable guidance in the application of finite strain theory to this problem. The computations presented here utilized the Extreme Science and Engineering Discovery Environment, which is supported by the National Science Foundation grant number OCI-1053575.

References

[1] R.O. Cleveland, J.A. McAteer, The physics of shock wave lithotripsy, in: A.D. Smith, G. Preminger, G. Badlani, L. Kavoussi (Eds.), Smith's Textbook on Endourology, Volume I, third ed., Wiley-Blackwell, 2012, pp. 529–558.
[2] M.R. Bailey, Y.A. Pishchalnikov, O.A. Sapozhnikov, R.O. Cleveland, J.A. McAteer, N.A. Miller, I.V. Pishchalnikova, B.A. Connors, L.A. Crum, A.P. Evan, Cavitation detection during shock-wave lithotripsy, Ultrasound. Med. Biol. 31 (2005) 1245–1256.
[3] E. Johnsen, T. Colonius, Shock-induced collapse of a gas bubble in shockwave lithotripsy, J. Acoust. Soc. Am. 124 (2008) 2011–2020.
[4] E. Johnsen, T. Colonius, Numerical simulations of non-spherical bubble collapse, J. Fluid. Mech. 629 (2009) 231–262.
[5] Y.A. Pishchalnikov, O.A. Sapozhnikov, M.R. Bailey, J.C. Williams, R.O. Cleveland, T. Colonius, L.A. Crum, A.P. Evan, J.A. McAteer, Cavitation bubble cluster activity in the breakage of kidney stones by lithotripter shockwaves, J. Endourol. 17 (2003) 435–446.
[6] C. Weber, M.E. Moran, E.J. Braun, G.W. Drach, Injury of rat renal vessels following extracorporeal shock wave treatment, J. Urol. 147 (1992) 476–481.
[7] P. Zhong, Y.F. Zhou, S.L. Zhu, Dynamics of bubble oscillation in constrained media and mechanisms of vessel rupture in SWL, Ultrasound Med. Biol 27 (2001) 119–134.
[8] H. Chen, A.A. Brayman, M.R. Bailey, T.J. Matula, Blood vessel rupture by cavitation, Urol. Res. 38 (2010) 321–326.
[9] H. Chen, W. Kreider, A.A. Brayman, M.R. Bailey, T.J. Matula, Blood vessel deformations on microsecond time scales by ultrasonic cavitation, Phys. Rev. Lett. 106 (2011).
[10] H. Chen, C. Perez, A.A. Brayman, T.J. Matula, High speed imaging of shockwave-induced dynamics of cavitation bubbles and vessel wall, J. Acoust. Soc. Am. 129 (2011) 2374.
[11] E.A. Brujan, K. Nahen, P. Schmidt, A. Vogel, Dynamics of laser-induced cavitation bubbles near an elastic boundary, J. Fluid. Mech. 433 (2001) 251–281.
[12] E.A. Brujan, K. Nahen, P. Schmidt, A. Vogel, Dynamics of laser-induced cavitation bubbles near elastic boundaries: influence of the elastic modulus, J. Fluid. Mech. 433 (2001) 283–314.
[13] T. Kodama, Y. Tomita, Cavitation bubble behavior and bubble-shock wave interaction near a gelatin surface as a study of in vivo bubble dynamics, Appl. Phys. B-Lasers O. 70 (2000) 139–149.
[14] C.F. Caskey, S.M. Stieger, S. Qin, P.A. Dayton, K.W. Ferrara, Direct observations of ultrasound microbubble contrast agent interaction with the microvessel wall, J. Acoust. Soc. Am. 122 (2007) 1191–1200.
[15] T. Ye, J.L. Bull, Microbubble expansion in a flexible tube, J. Biomech. Eng. Trans. ASME 128 (2006) 554–563.
[16] H. Miao, S.M. Gracewski, D. Dalecki, Ultrasonic excitation of a bubble inside a deformable tube: implications for ultrasonically induced hemorrhage, J. Acoust. Soc. Am. 124 (2008) 2374–2384.
[17] J.B. Freund, R.K. Shukla, A.P. Evan, Shock-induced bubble jetting into a viscous fluid with application to tissue injury in shock-wave lithotripsy, J. Acoust. Soc. Am. 126 (2009) 2746–2756.
[18] K. Kobayashi, T. Kodama, H. Takahira, Shock wave-bubble interaction near soft and rigid boundaries during lithotripsy: numerical analysis by the improved ghost fluid method, Phys. Med. Biol. 56 (2011) 6421–6440.
[19] J.-E. Blatteau, J.-B. Souraud, E. Gempp, A. Boussuges, Gas nuclei, their origin, and their role in bubble formation, Aviat. Space Environ. Med. 77 (2006) 1068–1076.
[20] L. Rayleigh, On the pressure developed in a liquid during the collapse of a spherical cavity, Phil. Mag. 34 (1917) 94–98.
[21] J.B. Freund, Suppression of shocked-bubble expansion due to tissue confinement with application to shock-wave lithotripsy, J. Acoust. Soc. Am. 123 (2008) 2867–2874.
[22] E. Johnsen, Numerical simulations of non-spherical bubble collapse with applications to shockwave lithotripsy, Ph.D. Thesis, California Institute of Technology, 2008.
[23] R.O. Cleveland, M.R. Bailey, N. Fineberg, B. Hartenbaum, M. Lokhandwalla, J.A. McAteer, B. Sturtevant, Design and characterization of a research electrohydraulic lithotripter patterned after the Dornier HM3, Rev. Sci. Instrum. 71 (2000) 2514–2525.
[24] K.M. Shyue, An efficient shock-capturing algorithm for compressible multi-component problems, J. Comput. Phys. 142 (1998) 208–242.
[25] S.A. Goss, R.L. Johnston, F. Dunn, Compilation of empirical ultrasonic properties of mammalian-tissues II, J. Acoust. Soc. Am. 68 (1980) 93–108.
[26] A. Gojani, K. Ohtani, K. Takayama, S. Hosseini, Shock Hugoniot and equations of states of water, castor oil, and aqueous solutions of sodium chloride, sucrose and gelatin, Shock Waves (2009) 1–6.
[27] G. Allaire, S. Clerc, S. Kokh, A five-equation model for the simulation of interfaces between compressible fluids, J. Comput. Phys. 181 (2002) 577–616.
[28] E. Johnsen, T. Colonius, Implementation of WENO schemes in compressible multicomponent flow problems, J. Comput. Phys. 219 (2006) 715–732.
[29] G.S. Jiang, C.W. Shu, Efficient implementation of weighted ENO schemes, J. Comput. Phys. 126 (1996) 202–228.
[30] C.W. Shu, S. Osher, Efficient implementation of essentially non-oscillatory shock-capturing schemes, J. Comput. Phys. 77 (1988) 439–471.
[31] E.F. Toro, M. Spruce, W. Speares, Restoration of the contact surface in the HLL-Riemann solver, Shock Waves 4 (1994) 25–34.
[32] D.S. Balsara, C.W. Shu, Monotonicity preserving weighted essentially non-oscillatory schemes with increasingly high order of accuracy, J. Comput. Phys. 160 (2000) 405–452.
[33] A.K. Henrick, T.D. Aslam, J.M. Powers, Mapped weighted essentially non-oscillatory schemes: achieving optimal order near critical points, J. Comput. Phys. 207 (2005) 542–567.
[34] K.W. Thompson, Time-dependent boundary-conditions for hyperbolic systems I, J. Comput. Phys. 68 (1987) 1–24.
[35] K.W. Thompson, Time-dependent boundary-conditions for hyperbolic systems II, J. Comput. Phys. 89 (1990) 439–461.
[36] E. Klaseboer, S.W. Fong, C.K. Turangan, B.C. Khoo, A.J. Szeri, M.L. Calvisi, G.N. Sankin, P. Zhong, Interaction of lithotripter shockwaves with single inertial cavitation bubbles, J. Fluid. Mech. 593 (2007) 33–56.
[37] A.R. Kemper, A.C. Santago, J.D. Stitzel, J.L. Sparks, S.M. Duma, Biomechanical response of human liver in tensile loading, Ann. Adv. Automot. Med. 54 (2010) 15–26.
[38] A.C. Santago, Characterizing the biomechanical response of the liver, Ph.D. Thesis, Virginia Polytechnic Institute and State University, 2010.
[39] M. Farshad, M. Barbezat, P. Flüeler, F. Schmidlin, P. Graber, P. Niederer, Material characterization of the pig kidney in relation with the biomechanical analysis of renal trauma, J. Biomech. 32 (1999) 417–425.
[40] J.G. Snedeker, P. Niederer, F.R. Schmidlin, M. Farshad, C.K. Demetropoulos, J.B. Lee, K.H. Yang, Strain-rate dependent material properties of the porcine and human kidney capsule, J. Biomech. 38 (2005) 1011–1021.